PEAKIT: A Gaussian Process regression analysis tool for chemical exchange saturation transfer spectra

Michele Lecis [a,b], Solène Bardin [a], Catalin I. Ciobanu [c], Luisa Ciobanu [a,*]

[a] *NeuroSpin, CEA, Gif-sur-Yvette, Paris-Saclay University, Saclay, France*
[b] *Technical University of Munich, Munich, Germany*
[c] *Boostrs SAS, Paris, France*

A B S T R A C T

Chemical Exchange Saturation Transfer (CEST) is a powerful technique for metabolic imaging, capable of exploring concentrations in the µM to mM range. However, extracting quantitative information from Z-spectra can be challenging due to the non-CEST contributions present and the limited knowledge about the exchanging pools. The *PEAKIT* tool is proposed as an alternative approach to quantifying CEST peaks, which requires no prior assumptions about the frequency offset or the underlying shape of the baseline. Specifically, the tool takes as input an experimental Z-spectrum and proceeds to identify peak candidates. After a baseline estimation based on Gaussian Process regression, *PEAKIT* outputs the chemical shift off-sets, the areas, the heights and the statistical significance of the detected peaks. The performance and limitations of the *PEAKIT* tool are discussed for *in vitro* and *in vivo* applications.

© 2021 The Author(s). Published by Elsevier Inc. This is an open access article under the CC BY license (http://creativecommons.org/licenses/by/4.0/).

1. Introduction

Chemical Exchange Saturation Transfer (CEST) has been successfully used for the *in vivo* detection of numerous metabolites including glutamate [1], glucose [2], creatine [3], lactate [4] and myoinositol [5]. The technique takes advantage of the exchange between the water protons and the protons within the metabolites of interest whose magnetization is selectively saturated for sufficiently long times to allow the subsequent saturation of the bulk water magnetization. The most straightforward way to analyse the CEST data is by computing the difference between the signals obtained upon radio frequency irradiations at two frequencies symmetric with respect to the water frequency, normalized to the signal obtained in the absence of saturation. This quantity, named CEST ratio or Magnetization Transfer Ratio Asymmetry (MTR_{asym}) [6], can be used to produce frequency-specific CEST maps. However, such maps fail to reflect CEST-only effects in the presence of confounding factors such as asymmetric magnetization transfer (MT) effects [7] or upfield Nuclear Overhauser Enhancement (NOE) effects [8]. The NOE effect is particularly problematic

for metabolites with CEST contributions in the 3 to 4 ppm range, as it has a large resonance peak at negative 3.5 ppm.

Alternative analysis methods model the measured spectral CEST signals (Z-spectra) as non-linear combinations of Lorentzian functions corresponding not only to the metabolites of interest, but also to the bulk water, the MT, and the NOE pools [9]. These approaches can extract information from overlapping peaks, but have the drawback that require a priori knowledge of the number of pools and their corresponding frequency shifts. Methods for finding the exchange rate and the labile proton ratio by fitting numerical or approximate analytical solutions of the Bloch-McConnell equations have also been proposed [10,11]. They typically require long acquisition times, can be computationally demanding, and may introduce errors due to the approximations made in using analytical solutions. Recently, the use of magnetic resonance finger printing (MRF) for CEST quantification has been reported both on phantoms and *in vivo* [12,13]. The accuracy of the results obtained with MRF depends on the size of the dictionaries used for matching the experimental CEST data. Deep neural networks can help improve this accuracy [14].

In this manuscript, we focus on developing a simple approach for detecting CEST peaks without making any assumptions about the frequency offset or the underlying line shape of the CEST

---

response. To this end, we have built a software tool (*PEAKIT*) which identifies statistically-significant peaks and calculates the peak height, area and statistical significance. The baseline, necessary for peak characterization, is estimated locally using a Gaussian Process regression model and is therefore minimally impacted by direct water saturation and NOE effects.

Compared to Lorentzian fits or the more complex Deep Neural Networks regression, Gaussian Processes (GP) are non-parametric models, well suited for problems in which the training data is relatively small. By construction GP predictions are not subject to large gradient variations which occasionally cause parametric models to diverge. One drawback of the GP approach is the associated computation time, which increases strongly with the number of training points considered. A comparison between GP and other machine learning methods is discussed in Ref. [15].

2. The *PEAKIT* software tool

PEAKIT was developed with Python 3.8 and provided with a user interface through the *tkinter* package (Fig. 1). The tool takes as input a spectrum consisting of saturation offsets on the *x* axis and the normalized signal intensities on the *y* axis, and it outputs the location (chemical shift offset) of each detected peak along with the peak's height, area and statistical significance (*p*-value). The user can specify whether the software should look for positive or negative peaks. By default, negative peaks are expected; in order to analyze positive peaks the box "up" has to be checked (see Fig. 1). There are three steps to the *PEAKIT* algorithm, corresponding to (i) the peak detection, (ii) the baseline estimation, and (iii) the *p*-value computation, respectively. A detailed description of each of these three steps is given in the following sections.

2.1. Peak detection

The peak detection process (Fig. 2) is based on an iterative approach exploiting the local properties of the spectrum [16].

Specifically, for each point i of coordinates (x_i, y_i), a slope α_i is computed as follows:

$$\alpha_i = \frac{y_{i+1} - y_i}{x_{i+1} - x_i}$$

Furthermore, at any point i we compute the moving average of the r preceding slopes as follows:

$$\bar{\alpha}_i = \frac{1}{r} \sum_{j=i-r-1}^{i-1} \alpha_j$$

where r is the number of consecutive points preceding point i. The appropriate choice of r depends on the noise level as well as on the shape of the spectrum: a dataset with numerous small peaks requires small values of r as the slope varies rapidly.

PEAKIT algorithm detects the apparition of a peak at point i_b (henceforth referred to as the *beginning of the peak*) if the following two conditions are met simultaneously:

$$\alpha_{i_b} - \bar{\alpha}_{i_b} > \Delta \tag{1a}$$

$$\alpha_{i_b+1} - \bar{\alpha}_{i_b} > \Delta \tag{1b}$$

where the threshold Δ is a free positive parameter which can be defined by the user. Specifically, in the *PEAKIT* tool, Δ is expressed as a percentage of the maximum α_i present in the spectrum; the user may input any Δ value between 0 and 100 (see Fig. 1). We make the following observations related to the choice of this parameter:
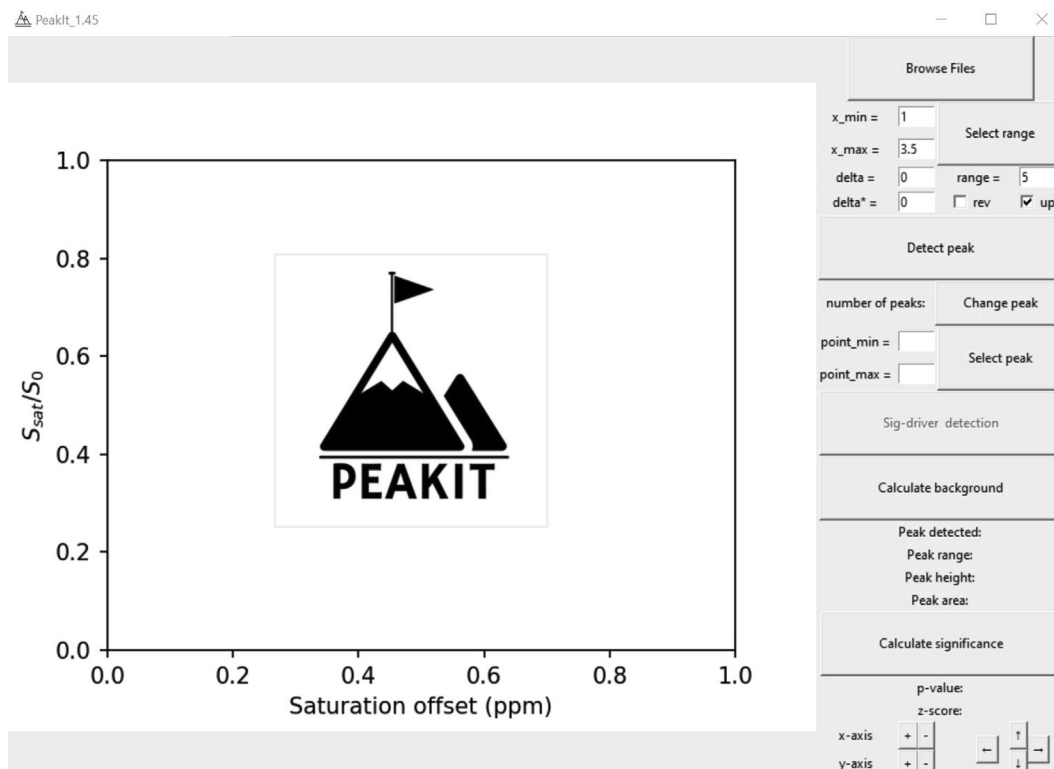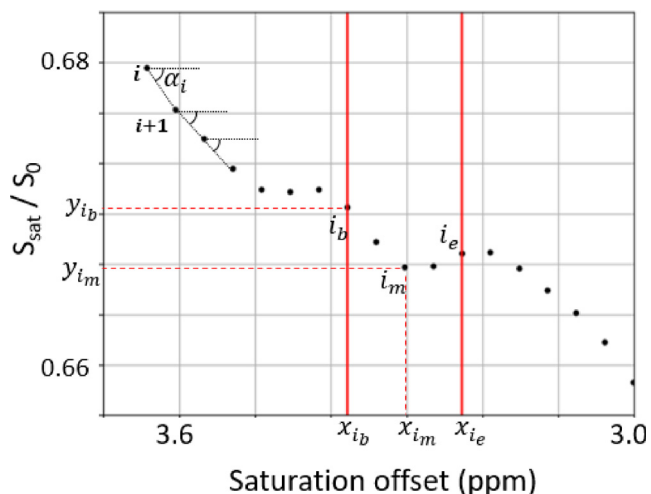

Fig. 1. Screenshot of the entry page of the *PEAKIT* software tool. The user can navigate the various functionalities from the panel on the right. The plot on the left displays the results and it updates according to the selection made by the user.

Fig. 2. Schematic representation of the peak detection process. The algorithm computes the slopes successively, checking at every step whether the peak conditions (1a) and (1b) are satisfied. For each identified peak, the algorithm outputs a set of three points: the beginning (i_b), the maximum (i_m), and the end (i_e) of the peak. The slopes α_i are defined in the text.

- Setting $\Delta = 0$ implies that a peak is detected when the slopes at two consecutive points i_b and $i_b + 1$ exceed the moving average at point i_b.
- In case of noisy shapes, two random fluctuations occurring consecutively may trigger the detection of a peak when none is in fact present. In these cases, setting a higher threshold Δ helps to reduce the rate of false positives and thus to improve the precision of peak detection.
- Finally, setting $\Delta = 100$ guarantees that neither of the conditions (1a) and (1b) will be met, and, as a result, no peak will be found.

As soon as the detection of a peak is triggered, the *PEAKIT* algorithm scans through the points $i_b + 1$, $i_b + 2$, ... until the peak maximum is reached at point i_m:

$$\alpha_{i_m} - \bar{\alpha_{i_b}} < \Delta^* \tag{2}$$

Thus, the maximum is detected when the slope is found to be smaller than the moving average recorded at the beginning of the peak ($\bar{\alpha_{i_b}}$), net of a threshold parameter Δ^*. The default value of Δ^* is set to 0, as in the most common cases it is sufficient that $\alpha_{i_{m+1}} - \bar{\alpha_{i_b}}$ is negative. In the case of adjacent and partially overlapping peaks it may be necessary to increase the Δ^* value (between 0 and 100) to prevent detecting multiple peaks as a single one. (Note: For positive peaks, the inequalities (1a), (1b) and (2) reverse signs.)

By default, the *PEAKIT* algorithm assumes the peak to be symmetric and adds an equal number of points to the right side of the peak maximum to complete peak detection. Thus, the end of the peak will occur at point $i_e = 2i_m - i_b$. In conclusion, the output of the peak detection process consists of a set of three points for each detected peak: i_b, i_m, and i_e corresponding to the beginning, the maximum, and the end of the peak, respectively. The "rev" checkbox (see Fig. 1) can be used to reverse the direction of the scan: for asymmetric peaks, the algorithm may perform better in one of the two directions (e.g., in case the discontinuity of the slope is more pronounced).

In cases in which the result of the automated peak detection algorithm is judged to be inaccurate, the selection of the peak can also be made manually, by entering the beginning and the

end values of the peak in the "point_min" and "point_max" fields, respectively. Regardless of how the peak was selected (automatically or manually), there is no impact on the subsequent steps of the analysis which include the baseline estimation and the peak significance computation, described in Sections 2.2 and 2.3, respectively.

2.2. Baseline estimation

In this section, we describe the baseline estimation for each detected peak. In essence, the baseline level estimates the shape of the spectrum if the detected peak were absent. Under this hypothesis, the baseline profile $\{b_i\}$ should match the spectrum $\{y_i\}$ located just outside the peak. To ensure this matching, our technique uses a set of $2r$ "training points" formed by the r points in the spectrum immediately preceding the peak, and the same number r of points immediately succeeding the peak.

The baseline estimation process relies on a Gaussian Process (GP) regression implemented via the *GPy* Python package [17]. An excellent introduction to Gaussian Processes can be found in Ref. [15]; this reference notably includes a chapter dedicated to GP regression which contains the full mathematical details of the method employed in *PEAKIT*. Without delving into these details, we mention that the GP technique produces, for all points $\{x_i\}$ within the peak region $i_b \leq i \leq i_e$, the predicted baseline levels $\{b_i\}$ along with their standard deviations $\{\sigma_i\}$ (Fig. 3). The values $\{\sigma_i\}$ form the uncertainty band around the predicted baseline shape. We note that the uncertainty band narrows as r increases. We also note that, for a given value of r, a noisier dataset $\{y_{i_b-r}, \cdots, y_{i_b-1}, y_{i_e+1}, \cdots, y_{i_e+r}\}$ will produce a wider uncertainty band.

Once the baseline level is established, it is possible to quantify how much of the height and area of the peak can be attributed to signal. These contributions are inferred from the observed data by subtracting the baseline estimation. In addition, we re-compute the peak center location by identifying the point i in the peak region of the spectrum for which the difference ($y_i - b_i$) is maximum.

2.3. Peak significance computation

The third and final goal of the *PEAKIT* tool is to compute a *p*-value for each detected peak. If the *p*-value is smaller than a certain
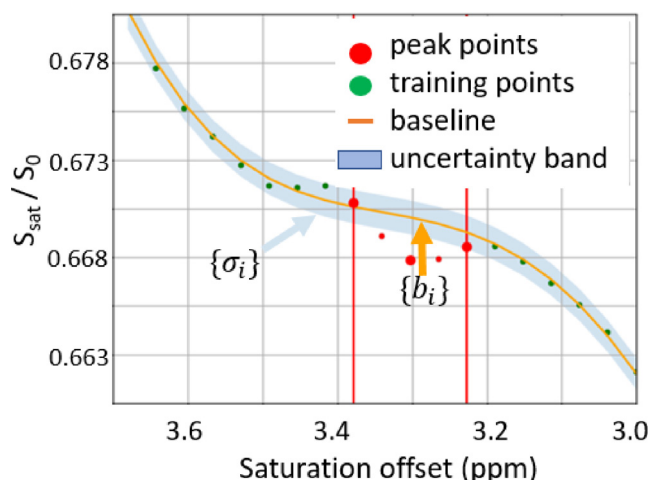
Fig. 3. Based on the training points (green markers), the GP regression produces, for all points in the peak region, a baseline shape $\{b_i\}$ (orange line) along with their standard deviations $\{\sigma_i\}$ (shaded band). (For interpretation of the references to colour in this figure legend, the reader is referred to the web version of this article.)
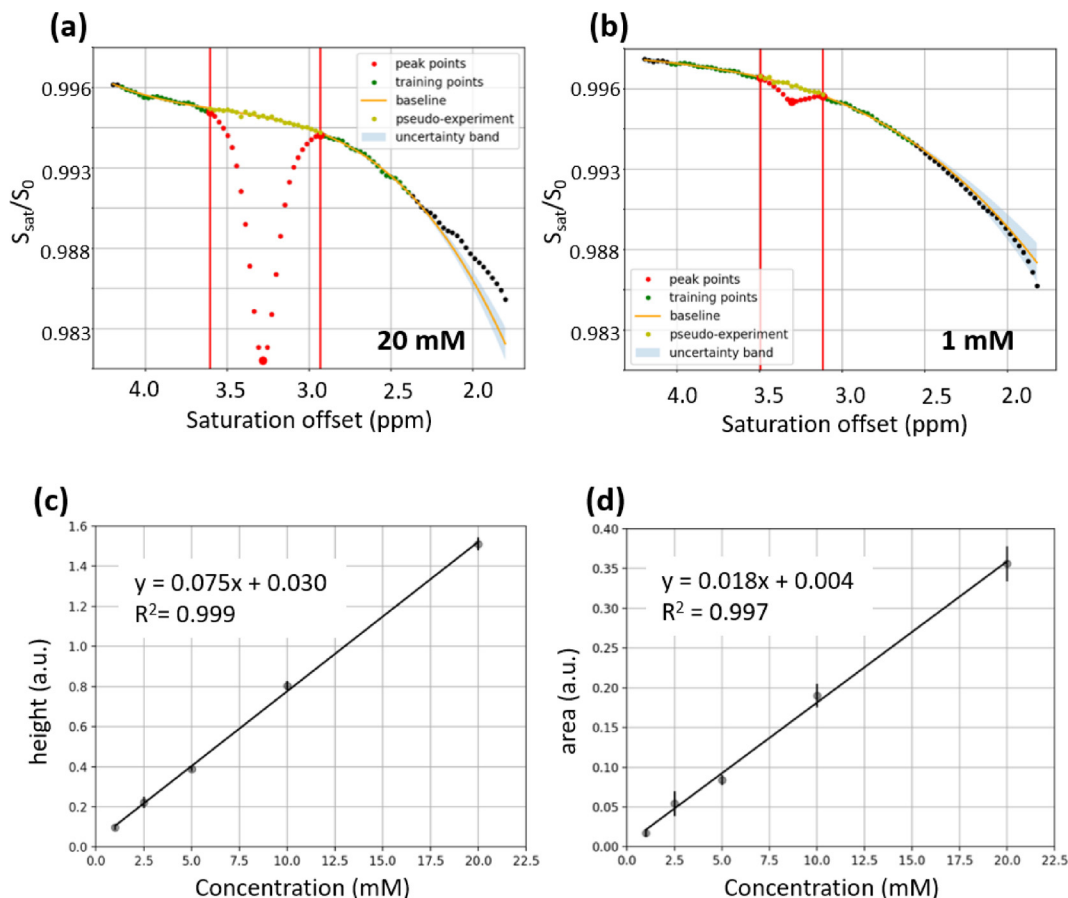
Fig. 4. Examples of *PEAKIT* analysis of Z-spectra acquired on carnosine phantoms in PBS at different concentrations: 20 mM (a) and 1 mM (b). The Z-spectra show a significant peak centered at 3.3 ppm. The peak height (c) and the peak area (d) increase linearly with the metabolite concentration. The Z-spectra were acquired with a nominal spectral resolution of 0.054 ppm (zero-filled to 0.027) using a saturation power B_1 = 1 μT. Each Z-spectrum is the average of 80 transients, for an acquisition time of 21 min.

threshold (for example, $p < 0.005$), then the detection of the given peak is confirmed. If, on the other hand, the p-value exceeds the threshold ($p > 0.005$) then the peak is not statistically significant, and is consequently discarded.

The significance assessment is based on the null hypothesis, which assumes the detected peak is not due to the CEST signal but is instead generated by random fluctuations of the noise around the baseline. In order to test the null hypothesis, noise fluctuations are randomly generated in a Monte Carlo simulation.

Specifically, at every point i in the peak region $i_b \leq i \leq i_e$ we generate a random number B_i from the Gaussian distribution whose mean and standard deviation are the predicted b_i and σ_i, respectively. The ensemble of values $\{B_i\}$ forms a *pseudo-experiment*, which is simply a spectrum randomly generated from the baseline shape according to its uncertainty band.

Next, we compute a measure of how consistent this pseudo-experiment is with the baseline data using a χ^2 approach:

$$\chi^2_{pseudo} = \sum_{i=i_b}^{i_e} \frac{(B_i - b_i)^2}{b_i}$$

The process is repeated N times to generate a large number of pseudo-experiments (for example, N = 100,000), and for each pseudo-experiment we record its corresponding χ^2 value calculated using the above equation. The larger its χ^2 value, the more the pseudo-experiment will have deviated from the baseline shape.

To estimate the p-value, we compute the fraction of pseudo-experiments which deviate from the baseline as much as the data or more, or in mathematical terms the fraction of pseudo-experiments having $\chi^2_{pseudo} \geq \chi^2_{data}$, where χ^2_{data} given by:

$$\chi^2_{data} = \sum_{i=i_b}^{i_e} \frac{(y_i - b_i)^2}{b_i}$$

where y_i are the experimental points and b_i are, as in the previous formulae, the baseline points predicted by the GP regression.

If the detected peak is generated by signal (as opposed to noise), then the experimental points will deviate significantly from the predicted baseline shape, resulting in a large value of χ^2_{data}. As consequence, very few pseudo-experiments, if any, will fluctuate to the level of the experimental data or more ($\chi^2_{pseudo} \geq \chi^2_{data}$) and the p-value will consequently be very small. This allows to reject the null hypothesis and confirm peak detection.

Finally, if none of the pseudo-experiments have $\chi^2_{pseudo} \geq \chi^2_{data}$, this implies that the number of pseudo-experiments N is insufficient for extracting a precise p-value, and an upper bound can be set: $p < \frac{1}{N}$. For example, if N = 100,000 and we register no pseudo-experiments with $\chi^2_{pseudo} \geq \chi^2_{data}$ then we conclude that the p-value satisfies $p < 0.001\%$. As a general rule, choosing an appropriate number N of pseudo-experiments is a trade-off between ensuring a high statistical precision (larger N is better) and maintaining a short computation time (smaller N is better).
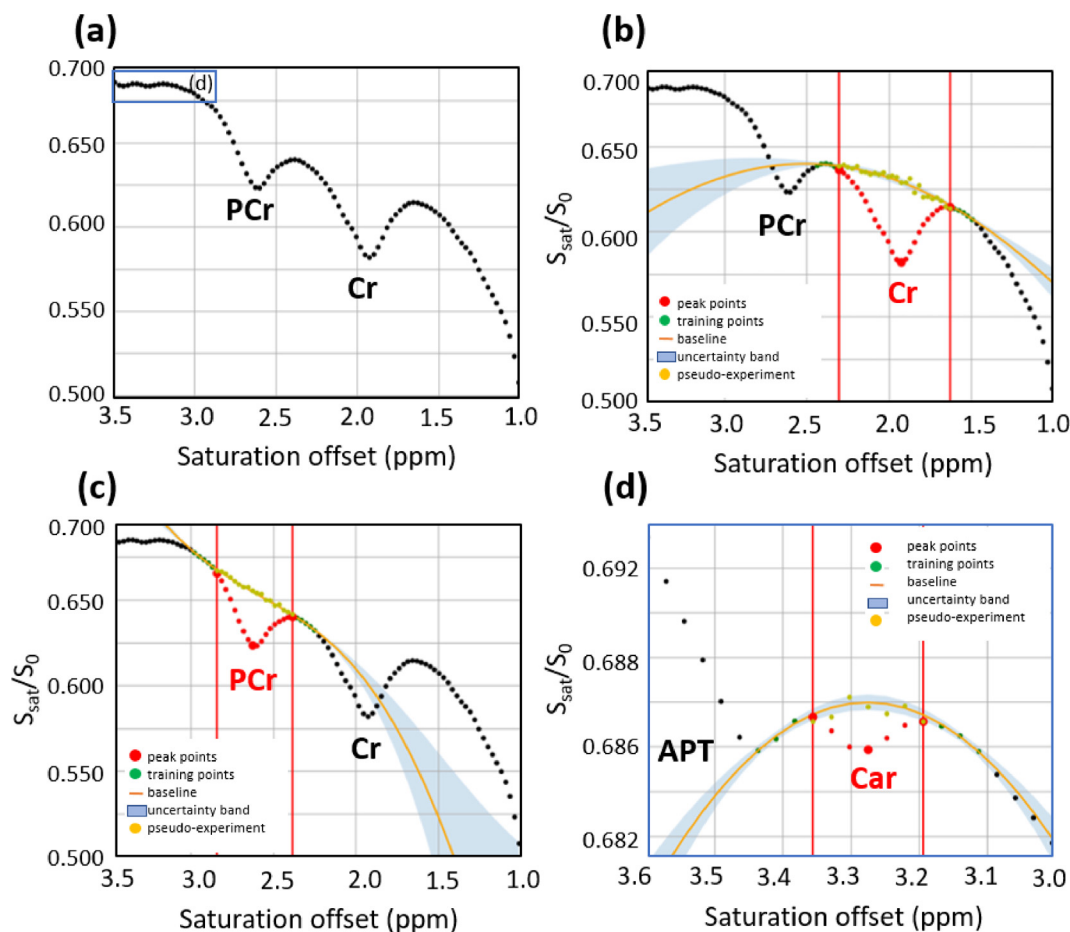
Fig. 5. *PEAKIT* analysis of a Z-spectrum acquired *in vivo* on a rat leg muscle. (a) Downfield region of the spectrum in which are apparent four significant CEST peaks corresponding to creatine, phosphocreatine, carnosine and APT. The analyses of the creatine and phosphocreatine CEST peaks are shown in (b) and (c), respectively. (d) Zoom on the 3.0 – 3.6 ppm range showing the *PEAKIT* analysis of the carnosine CEST peak. The Z-spectrum was acquired with a nominal spectral resolution of 0.054 ppm (zero-filled to 0.027) using a saturation power $B_1 = 1\mu T$. Each Z-spectrum is the average of 80 transients, for an acquisition time of 21 min.

Table 1
PEAKIT output obtained on the Z-spectrum in Fig. 5.

Metabolite	Peak frequency offset (ppm)	Height (a.u.)	Area (a.u.)	*p*-value
Creatine	1.93	4.8 ± 0.4	1.55 ± 0.2	$<5 \cdot 10^{-7}$
Phosphocreatine	2.63	3.6 ± 0.1	$(9.3 ± 0.5) \cdot 10^{-1}$	$<5 \cdot 10^{-7}$
Carnosine	3.28	$(4.1 ± 0.4) \cdot 10^{-1}$	$(4.2 ± 0.6) \cdot 10^{-2}$	$<5 \cdot 10^{-7}$
APT	3.46	$(3.8 ± 1.5) \cdot 10^{-1}$	$(4.2 ± 2.4) \cdot 10^{-2}$	$3.7 \cdot 10^{-3}$

3. Applications

To evaluate the performance of *PEAKIT* we analyzed CEST spectra acquired on a 17.2 T pre-clinical scanner (Bruker Biospin, Germany). The CEST acquisitions were performed using an in-house written linescan CEST pulse sequence developed according to Ref. [18]. The pulse sequence and all experimental parameters are described in detail in Ref. [19]. For the *in vivo* experiments, all animal procedures were approved by the French authorities, notably by the Comité d'Ethique en Expérimentation Animale, Commissariat à l'Energie Atomique et aux Énergies Alternatives, and the Ministère de l'Education Nationale, de l'Enseignement Supérieur et de la Recherche under reference A15 − 40 and were conducted in strict accordance with the recommendations and guidelines of the European Union (Directive 2010/63/EU) and the French National Committee (Décret 2013–118).

3.1. In vitro detection

PEAKIT was used to analyze Z-spectra acquired on phantom samples containing carnosine, known to present a CEST effect [20], in phosphate buffer solution (PBS) at pH = 7.2, and temperature 37 °C, at different concentrations (20 mM, 10 mM, 5 mM, 2.5 mM and 1 mM)

According to the results of the automatic detection, all the phantoms present a peak centered at 3.3 ppm, as expected. For baseline estimation thirty training points (*r* = 15) are used. The choice of this relatively large number of training points is motivated by the fact that there are no other contributions expected in the spectrum besides carnosine. Consequently, the uncertainty around the predicted baseline is narrow (Fig. 4a and 4b) and the fluctuations generated through pseudo-experiments are small compared to the peaks, resulting in *p*-values $p < 5 \cdot 10^{-7}$ for all concentrations studied.

In addition to position and significance, *PEAKIT* calculates the height and the area of each peak. As shown in Fig. 4c and d, both the height and the area are linearly correlated with the carnosine concentration. We stress here that although these linear fits can be used to infer the carnosine concentration from the CEST response of other similar samples, they cannot be used to unambiguously quantify the amount of carnosine present in samples with a very different composition (e.g. tissue samples). The estimation of the baseline, and therefore the estimated area and height of each peak, are dependent on the local shape of the Z-spectrum, which in turn depends on the sample (presence of MT or multiple peaks, for example) and the experimental parameters. Thus, *PEAKIT* is suited to conducting *semi-quantitative* analyses and comparisons between spectra generated by very similar samples, and acquired under the same experimental conditions.

3.2. In vivo detection

To test the performance of the *PEAKIT* for *in vivo* acquisitions we analyzed a Z-spectrum acquired on a rat leg muscle. On the left side of the spectrum (downfield) we can identify four peaks (Fig. 5a). At 1.9 and 2.6 ppm we recognize creatine (Cr) and phosphocreatine (PCr) [21]. Due to the asymmetric shape of the peaks, the automatic detection is manually adjusted to the range 2.32–1.64 ppm for Cr (Fig. 5b) and 2.85–2.32 ppm for PCr (Fig. 5c). The baseline is estimated considering five training points per side ($r = 5$) and the significance assessment returns a *p*-value $< 5 \cdot 10^{-7}$ for both peaks, confirming the detection. The peak detected at 3.3 ppm is attributable to carnosine [19], with a *p*-value $p < 5 \cdot 10^{-7}$. The parameter r is lowered to 4, due to the smaller number of points in the peak (Fig. 5d). The amide proton transfer (APT) peak [22], centered at 3.5 ppm was also found significant ($p = 3.7 \cdot 10^{-3}$). The output results from the *PEAKIT* analysis of the four peaks are summarized in Table 1.

4. Conclusion

We report the development and testing of *PEAKIT* - a software tool for the detection and characterization of CEST peaks. The performance of the tool was evaluated through the analysis of *in vitro* and *in vivo* CEST data acquired at 17.2 T using a linescan CEST pulse sequence. The tool is not intended for the detection of highly overlapping peaks for which other analysis approaches should be employed [9,11]. Compared to other existing tools used for the detection and characterization of CEST peaks, *PEAKIT* has the advantage that it does not require assumptions regarding the position and the shape of the peaks. The software is easy to use and of reduced computational cost.

For each detected peak, *PEAKIT* returns its height, area, and statistical significance. While these are quantitative measures characterizing the signal, care must be in exerted when interpreting the analysis results. Specifically, these variables as well as other similar CEST metrics [23] depend on the RF saturation power levels, the B_0 field strength, the exchange rates, and the local shape of the Z-spectrum. As a result, one cannot directly compare results obtained from samples having very different molecular composition (e.g. metabolites in solutions vs tissue samples). Absolute quantification is possible, however, if an a priori calibration is available, under the same experimental conditions. We note that *PEAKIT* can be a helpful tool in the characterization of new CEST agents. For *in vivo* applications, *PEAKIT* can be used to monitor metabolic dynamic processes.

The *PEAKIT* software is open-source, and freely available for download from github [24].

Declaration of Competing Interest

The authors declare that they have no known competing financial interests or personal relationships that could have appeared to influence the work reported in this paper.

References

[1] K. Cai et al., Magnetic resonance imaging of glutamate, Nat. Med. 18 (2) (2012) 302–306, https://doi.org/10.1038/nm.2615.

[2] X. Xu et al., ᴅ -glucose weighted chemical exchange saturation transfer (glucoCEST)-based dynamic glucose enhanced (DGE) MRI at 3T: early experience in healthy volunteers and brain tumor patients, Magn. Reson. Med. 84 (1) (2020) 247–262, https://doi.org/10.1002/mrm.28124.

[3] M. Haris et al., Exchange rates of creatine kinase metabolites: feasibility of imaging creatine by chemical exchange saturation transfer MRI, NMR Biomed. 25 (11) (2012) 1305–1309, https://doi.org/10.1002/nbm.2792.

[4] C. DeBrosse et al., Lactate Chemical Exchange Saturation Transfer (LATEST) Imaging in vivo: a biomarker for LDH activity, Sci. Rep. 6 (1) (2016), https://doi.org/10.1038/srep19517.

[5] M. Haris, K. Cai, A. Singh, H. Hariharan, R. Reddy, In vivo mapping of brain myo-inositol, NeuroImage 54 (3) (2011) 2079–2085, https://doi.org/10.1016/j.neuroimage.2010.10.017.

[6] P.Z. Sun, Simplified and scalable numerical solution for describing multi-pool chemical exchange saturation transfer (CEST) MRI contrast, J. Magn. Reson. 205 (2) (2010) 235–241, https://doi.org/10.1016/j.jmr.2010.05.004.

[7] J. Hua, C.K. Jones, J. Blakeley, S.A. Smith, P.C.M. van Zijl, J. Zhou, Quantitative description of the asymmetry in magnetization transfer effects around the water resonance in the human brain, Magn. Reson. Med. 58 (4) (2007) 786–793, https://doi.org/10.1002/mrm.21387.

[8] P.C.M. van Zijl, N.N. Yadav, Chemical exchange saturation transfer (CEST): What is in a name and what isn't?, Magn Reson. Med. 65 (4) (2011) 927–948, https://doi.org/10.1002/mrm.22761.

[9] M. Zaiss, B. Schmitt, P. Bachert, Quantitative separation of CEST effect from magnetization transfer and spillover effects by Lorentzian-line-fit analysis of z-spectra, J. Magn. Reson. 211 (2) (2011) 149–155, https://doi.org/10.1016/j.jmr.2011.05.001.

[10] M.T. McMahon, A.A. Gilad, J. Zhou, P.Z. Sun, J.W.M. Bulte, P.C.M. van Zijl, Quantifying exchange rates in chemical exchange saturation transfer agents using the saturation time and saturation power dependencies of the magnetization transfer effect on the magnetic resonance imaging signal (QUEST and QUESP): Ph calibration for poly-L-lysine and a starburst dendrimer, Magn. Reson. Med. 55 (4) (2006) 836–847, https://doi.org/10.1002/mrm.20818.

[11] M. Zaiss, G. Angelovski, E. Demetriou, M.T. McMahon, X. Golay, K. Scheffler, QUESP and QUEST revisited - fast and accurate quantitative CEST experiments: QUESP and QUEST Revisited, Magn. Reson. Med. 79 (3) (2018) 1708–1721, https://doi.org/10.1002/mrm.26813.

[12] O. Cohen, S. Huang, M.T. McMahon, M.S. Rosen, C.T. Farrar, Rapid and quantitative chemical exchange saturation transfer (CEST) imaging with magnetic resonance fingerprinting (MRF): Cohen et al, Magn. Reson. Med. 80 (6) (2018) 2449–2463, https://doi.org/10.1002/mrm.27221.

[13] O. Perlman, K. Herz, M. Zaiss, O. Cohen, M.S. Rosen, C.T. Farrar, CEST MR-Fingerprinting: practical considerations and insights for acquisition schedule design and improved reconstruction, Magn. Reson. Med. 83 (2) (2020) 462–478, https://doi.org/10.1002/mrm.27937.

[14] B. Kim, M. Schär, H. Park, H.-Y. Heo, A deep learning approach for magnetization transfer contrast MR fingerprinting and chemical exchange saturation transfer imaging, NeuroImage 221 (2020), https://doi.org/10.1016/j.neuroimage.2020.117165 117165.

[15] C.E. Rasmussen, C.K.I. Williams, Gaussian processes for machine learning, MIT Press, In accordance with Chapter 2 ("Regression"), we have selected a squared-exponential covariance function whose hyperparameters are determined from the training data using a maximum likelihood method.

[16] S.V. Chekanov, M. Erickson, A nonparametric peak finder algorithm and its application in searches for new physics, Adv. High Energy Phys. 2013 (2013) 1–4, https://doi.org/10.1155/2013/162986.

[17] GPy, GPy: A Gaussian process framework in python, 2018, http://github.com/SheffieldML/GPy.

[18] X. Xu, J.-S. Lee, A. Jerschow, Ultrafast scanning of exchangeable sites by NMR spectroscopy, Angew. Chem. Int. Ed. 52 (32) (2013) 8281–8284, https://doi.org/10.1002/anie.201303255.

[19] S. Bardin, M. Lecis, D. Boido, F. Boumezbeur, L. Ciobanu, First in vivo detection of carnosine using CEST, in: Presented at the ISMRM, Montréal, QC, Canada, May 2021.

[20] O. Bodet, S. Goerke, N.G.R. Behl, V. Roeloffs, M. Zaiss, P. Bachert, Amide proton transfer of carnosine in aqueous solution studied *in vitro* by WEX and CEST experiments: study of amide proton transfer in carnosine-water system, NMR Biomed. 28 (9) (2015) 1097–1103, https://doi.org/10.1002/nbm.3343.

[21] K. Pavuluri, J.T. Rosenberg, S. Helsper, S. Bo, M.T. McMahon, Amplified detection of phosphocreatine and creatine after supplementation using CEST MRI at high and ultrahigh magnetic fields, J. Magn. Reson. 313 (Apr.) (2020), https://doi.org/10.1016/j.jmr.2020.106703 106703.

[22] J. Zhou, J.-F. Payen, D.A. Wilson, R.J. Traystman, P.C.M. van Zijl, Using the amide proton signals of intracellular proteins and peptides to detect pH effects in MRI, Nat. Med. 9 (8) (2003) 1085–1090, https://doi.org/10.1038/nm907.

[23] H. Heo et al., Insight into the quantitative metrics of chemical exchange saturation transfer (CEST) imaging, Magn. Reson. Med. 77 (5) (2017) 1853–1865, https://doi.org/10.1002/mrm.26264.

[24] https://github.com/SKMikee/PeakIt.